PHYSICAL REVIEW A **84**, 033842 (2011)

Mechanism and computational model for Lyman-α-radiation generation by high-intensity-laser four-wave mixing in Kr-Ar gas

Oleg A. Louchev,[1,*] Pavel Bakule,[2] Norihito Saito,[1] Satoshi Wada,[1] Koji Yokoyama,[1,3] Katsuhiko Ishida,[3] and Masahiko Iwasaki[3]
[1]*Advanced Science Institute, RIKEN, 2-1 Hirosawa, Wako, Saitama, 351-0198, Japan*
[2]*STFC, ISIS Facility, Rutherford Appleton Laboratory, Chilton, Oxfordshire OX11 0QX, United Kingdom*
[3]*Advanced Meson Science Laboratory, RIKEN Nishina Center, RIKEN, Wako, Saitama 351-0198, Japan*

(Received 12 November 2010; published 20 September 2011)

We present a theoretical model combined with a computational study of a laser four-wave mixing process under optical discharge in which the non-steady-state four-wave amplitude equations are integrated with the kinetic equations of initial optical discharge and electron avalanche ionization in Kr-Ar gas. The model is validated by earlier experimental data showing strong inhibition of the generation of pulsed, tunable Lyman-α (Ly-α) radiation when using sum-difference frequency mixing of 212.6 nm and tunable infrared radiation (820–850 nm). The rigorous computational approach to the problem reveals the possibility and mechanism of strong auto-oscillations in sum-difference resonant Ly-α generation due to the combined effect of (i) 212.6-nm (2+1)-photon ionization producing initial electrons, followed by (ii) the electron avalanche dominated by 843-nm radiation, and (iii) the final breakdown of the phase matching condition. The model shows that the final efficiency of Ly-α radiation generation can achieve a value of $\sim 5\times10^{-4}$ which is restricted by the total combined absorption of the fundamental and generated radiation.

DOI: 10.1103/PhysRevA.84.033842 PACS number(s): 42.65.Ky, 42.65.Sf

I. INTRODUCTION

Nonlinear laser wave mixing in gases [1] and solids [2] has been for many years a focus of optics research into extending the operating wavelengths of existing laser systems from infrared to visible, ultraviolet (UV), and vacuum UV (VUV) ranges. In making the up-conversion to short wavelengths below 160 nm, strong absorption in solid nonlinear media has to be avoided, leading to use of gaseous media and, therefore, low-efficiency $\chi^{(3)}$ processes. Progress in this field requires overcoming various limitations [3–10] in order to obtain higher wave-mixing efficiencies and output powers. In this connection we note the phenomenon of electromagnetically induced transparency introduced by Harris *et al.* [6] and reviewed in detail recently in Ref. [11]. This phenomenon effectively allows one to enhance four-way mixing in gases via coherent preparation of the quantum states of atoms and molecules.

In our present work we reexamine the four-wave mixing process focusing on a comprehensive modeling of four-wave mixing for generation of VUV Lyman-α (Ly-α) radiation using the classical resonant scheme. Ly-α radiation is important for a number of reasons. First, both pulsed and continuous Ly-α laser sources are required for efficient laser cooling via $1S$-$2P$ transition in H-like atoms [12–16]. Second, Ly-α radiation can be used for advanced lithography applications [17]. Third, pulsed tunable Ly-α radiation of a few dozen mJ and $\tau_p \approx 1$ ns pulse duration is required for efficient generation of ultralow-energy polarized positive muons (LE-μ^+), which are used as local magnetic microprobes on the nanometer scale in solid-state physics and surface and materials sciences using the LE-μ^+ spin rotation and resonance (LE-μSR) technique [18–22]. The LE-μ^+ are produced via Ly-α resonant $1S$-$2P$-unbound ionization of thermal energy muonium atoms. High-energy Ly-α pulses are useful for generating an intense LE-μ^+ (10^3–10^6 μ^+/s) which would not only open up the field of LE-μSR to a wider range of experiments but also allow a very fundamentally precise measurement of the muon anomalous magnetic moment to the level of 0.1 ppm in order to provide a test of the standard model of particle physics.

Four-wave mixing in gases has had many experimental and theoretical contributions [9–17,19–36] focused on various effects below the optical discharge threshold of $\sim 10^{11}$–10^{12} W/cm^2 and under plasma conditions [37]. We consider here a sum-difference process with two photons of $\lambda_1 = 212.6$-nm and one photon of $\lambda_2 = 815$–850-nm radiation to produce Ly-α radiation ($\lambda_3 = 121.5$–122.2 nm) where the phase matching condition, $\Delta k = 2k_1 – k_2 – k_3 \approx 0$, is achieved by a proper mixing of the negatively dispersive Kr and positively dispersive Ar (at λ_3). This technique of phase matching has been well known for many years [1] and was experimentally checked for four-wave mixing in Kr-Ar [19,25] and recently in Ar-Xe mixtures [38] for optimizing low-intensity generation. However, any attempt to use the initially phase-matched gas mixtures for high-intensity and high-efficiency generation faces the problem of optically induced discharge followed by electron avalanche, change of the refractive indices, and thereby breakdown of the phase matching condition.

The optics of four-wave mixing in various approximations and many aspects and pathways of laser ionization and plasma generation have been studied in various publications and considered in a few review papers and monographs [1,2,11,37,39,40]. However, the interplay of multiple laser frequencies and related physical effects significantly complicates the estimation of process efficiency, the prediction of the discharge threshold, and prediction of plasma development conditions that will disable operation. In our present work we develop a complex numerical model which integrates the nonlinear

---

[*] Corresponding author: oleglouchev@riken.jp

optics formalism with the various mechanisms of initial optical ionization and equations of laser-induced electron avalanche in Kr-Ar plasma. This coupled model reveals important features of this process, permits interpretation of previous experiments, and predicts additional effects. First, this model and simulation clearly explains the efficiency inhibition taking place with increase in the input irradiation observed in experiments on pulsed nanosecond Ly-α generation [36]. Second, this model and simulation allows us to identify effective pathways for producing the initial ionization and electron avalanche during operation. Third, the model reveals a basic mechanism for the onset of auto-oscillations of the generated radiation. Finally, the model shows that in the pulsed mode high efficiency can be achieved even with operation near and under the optical discharge threshold if the high electron density and dephasing develop at the final stage of the pulse duration and, therefore, do not lead to Ly-α pulse inhibition.

II. NONLINEAR OPTICS MODEL

In particular, we consider a four-wave mixing process with a resonant enhancement of the third-order susceptibility, $\chi^{(3)}$, in Kr phase-matched by Ar as schematically shown in Fig. 1. In order to couple the nonlinear optical process with optical discharge phenomena we consider a space where the fundamental λ_1 and λ_2 TEM$_{00}$ laser beams are collimated into a focal volume of a given radius r_0 and length L. We consider energy transfer from the narrow-bandwidth fundamental laser sources into the Ly-α (λ_3) radiation within the slowly varying amplitude approximation (SVA) [1,2]. We take into account the saturation mechanism suggested by Boyd *et al.* [5] as well as various types of linear and two-photon absorption (TPA). The laser intensities I_i along the beam direction z, associated with the wave amplitudes by $A_i(r,z,t) = [I_i(r,z,t)/2n_i\varepsilon_0 c]^{1/2}$, simulated in SVA approximation are described by the following set of equations [1,2,5]:

$$\frac{1}{V_{g1}}\frac{\partial A_1}{\partial t} + \frac{\partial A_1}{\partial z} = \frac{i\omega_1^2}{k_1 c^2}\left(\chi^{(3)} A_2 A_3 A_1^* e^{-i\Delta kz} + 2\chi_s^{\mathrm{TPA}} A_1^3\right) - \frac{1}{2}\alpha_1 A_1 - \frac{1}{2}\alpha_1^* A_1 - \frac{1}{2}\beta_{1-1}^* A_1^3, \quad (1)$$

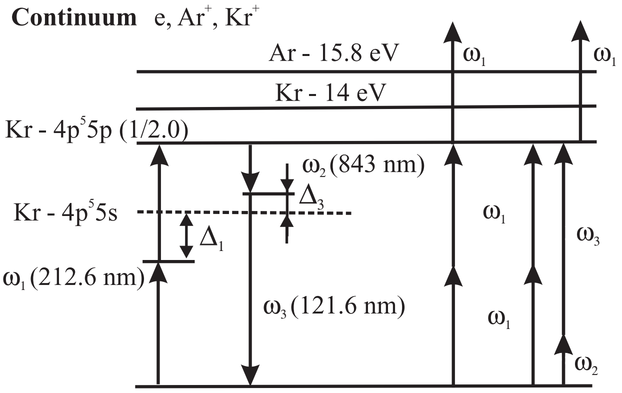

FIG. 1. Energy-level diagram of the resonant wave mixing in Kr phase-matched with Ar and related absorption processes. $\Delta_1 = 4.23$ eV; $\Delta_3 = 0.16$ eV.

$$\frac{1}{V_{g2}}\frac{\partial A_2}{\partial t} + \frac{\partial A_2}{\partial z} = \frac{1}{2}\frac{i\omega_2^2}{k_1 c^2}\left(\chi^{(3)} A_1^2 A_3^* e^{i\Delta kz} + 2\chi_D^{\mathrm{TPA}} A_3^2 A_2\right) - \frac{1}{2}\alpha_2 A_2 - \frac{1}{2}\beta_{2-3}^* A_3^2 A_2, \quad (2)$$

$$\frac{1}{V_{g3}}\frac{\partial A_3}{\partial t} + \frac{\partial A_3}{\partial z} = \frac{1}{2}\frac{i\omega_3^2}{k_3 c^2}\left(\chi^{(3)} A_1^2 A_2^* e^{i\Delta kz} + 2\chi_D^{\mathrm{TPA}} A_2^2 A_3\right) - \frac{1}{2}\alpha_3 A_3 - \frac{1}{2}\beta_{3-2}^* A_2^2 A_3, \quad (3)$$

where $A_i(r,0,t) = [I_{0i} f_{ri}(r) f_{ti}(t)/2n_i\varepsilon_0 c]^{1/2}$ for $i = 1,2$ and $A_3 = 0$ where $f_{ri}(r) = \exp(-r^2/r_{0i}^2)$ and $f_{it}(t)$ are the radial distribution and time dependence of the input laser beams, $\varepsilon_0 = 8.85\times10^{-12}$ F/m, $V_{\mathrm{gi}} = c/n_\mathrm{i}$, $k_\mathrm{i} = n_\mathrm{i}\omega_\mathrm{i}/c$ is the wave vector, $\Delta k = 2k_1 – k_2 – k_3$ is the wave vector mismatch, $n_i = 1 + a_i N_{\mathrm{Kr}} + b_i N_{\mathrm{Ar}}$ is the refractive index of Kr-Ar gas with densities N_{Kr} and N_{Ar} [24], α_i is the linear absorption coefficient due to the free electrons, α_1^* is the linear absorption coefficient associated with one-photon ionization of Kr and Ar atoms excited previously by the resonant TPA (only Kr) or by collisions with electrons (Kr and Ar), $\beta_{1-1}^* = 2n_1\varepsilon_0 c\beta_{1-1}$ and β_{1-1} is the $\omega_1 + \omega_1$ resonant two-photon absorption (TPA) coefficient, $\beta_{2-3}^* = 2n_1\varepsilon_0 c\beta_{2-3}$, $\beta_{3-2}^* = 2n_1\varepsilon_0 c\beta_{3-2}$, and $\beta_{3-2} = \beta_{2-3}\omega_2/\omega_3$ are combined $\omega_2 + \omega_3$ resonant TPA coefficients [1], $\chi^{(3)} = \chi_{a-\mathrm{Kr}}^{(3)} N_{\mathrm{Kr}}$, where $\chi_{a-\mathrm{Kr}}^{(3)} = 1.1\times10^{-36}$ cm^6/erg [24]. For $N_{\mathrm{Kr}0} = 2.4\times10^{19}$ cm^{-3} ($P_{\mathrm{Kr}} = 10^5$ Pa) one finds $\chi^{(3)} = \chi_{a-\mathrm{Kr}}^{(3)} N_{\mathrm{Kr}0} = 2.66\times10^{-17}$ cm^3/erg $= 3.7\times10^{-25}$ m^2/V^2, $\chi_s^{\mathrm{TPA}} = \chi^{(3)}\Delta_3/\Delta_1 = 0.038\chi^{(3)}$, and $\chi_d^{\mathrm{TPA}} = \chi^{(3)}\Delta_1/\Delta_3 = 26.43\chi^{(3)}$.

The linear absorption coefficient associated with the free electrons is given by [40]

$$\alpha_i \approx \frac{\nu_c\omega_p^2}{c(\omega_i^2 + \nu_c^2)} \approx \frac{\nu_c\omega_p^2}{c\omega_i^2}, \quad (4)$$

where $\omega_p = (e^2 N_e/\varepsilon_0 m)^{1/2}$ is the plasma frequency, N_e is the electron density, m is the electron mass, and e is the electron charge; $\nu_c \approx (N_{\mathrm{Kr}} + N_{\mathrm{Ar}})\sigma\bar{V}_{\mathrm{el}} = 10^{10}$–$10^{11}$ Hz ($\ll\omega_\mathrm{i}$) is the frequency with which the electron collides with the Kr or Ar atoms, $\sigma \approx 2\times10^{-16}$ cm^2 is the collision cross section [41], and $\bar{V}_{\mathrm{el}} = (8kT_e/\pi m_e)^{1/2} \approx 1.2$–$1.8\times10^8$ cm/s is the mean electron velocity for the electron energy 5–10 eV.

Kr atoms are assumed to be excited by the resonant $\omega_1 + \omega_1$ TPA with coefficient $\beta_{1-1} = \beta_0 N_{\mathrm{Kr}}/N_{\mathrm{Kr}0}$, where $\beta_0 \approx \sigma^{(2)} N_{\mathrm{Kr}0}/\hbar\omega_1 \approx 2.6$–$6.5\times10^{-13}$ cm/W for $N_{\mathrm{Kr}0} = 2.4\times10^{19}$ cm^{-3} and $\sigma^{(2)} \approx (1$–$2.5)\times10^{-50}$ cm^4 s/photon^2 [2]. The value of $\beta_0 \approx \sigma^{(2)} N_{\mathrm{Kr}0}/\hbar\omega_1 \approx 6.5\times10^{-13}$ cm/W for $\sigma^{(2)} \approx 2.5\times10^{-50}$ cm^4 s/photon^2 agrees well with that given by the expression of the two-photon coefficient via $\chi^{(3)}$: $\beta_0 \approx 2\omega_1\chi^{(3)}/n_1^2\varepsilon_0 c^2 \approx 8\times10^{-13}$ cm/W (for $N_{\mathrm{Kr}0} = 2.4\times10^{19}$ cm^{-3}). For the combined $\omega_2 + \omega_3$ resonant TPA coefficients we use $\beta_{2-3} \approx \sigma^{(2)} N_{\mathrm{Kr}0}/\hbar\omega_2 \approx 2.6\times10^{-12}$ cm/W and $\beta_{3-2} = \beta_{2-3}\omega_2/\omega_3 \approx 3.6\times10^{-13}$ cm/W for $\sigma^{(2)} \approx 2.5\times10^{-50}$ cm^4 s/photon^2 and $N_{\mathrm{Kr}0} = 2.4\times10^{19}$ cm^{-3}.

The coefficient for one-photon absorption by the exited Kr and Ar atoms is defined by

$$\alpha_1^* = \sigma_{\mathrm{Kr}}^* N_{\mathrm{Kr}}^* + \sigma_{\mathrm{Ar}}^* N_{\mathrm{Ar}}^*, \qquad (5)$$

where $\sigma_{\mathrm{Kr}}^* \approx \sigma_{\mathrm{Ar}}^* \approx 4\times10^{-18}$ cm^2 is the absorption cross section for the excited state [42] and N_{Kr}^* and N_{Ar}^* are the densities of excited Kr and Ar atoms. (Ar atoms can be only excited by the electron collisions with the rate specified in Sec. III).

III. PLASMA GENERATION MODEL

In coupling the previously mentioned nonlinear optical process with a plasma model we take into account the densities of electrons (N_e), Kr atoms (N_{Kr}), Ar atoms (N_{Ar}), excited Kr atoms (N_{Kr}^*), excited Ar atoms (N_{Kr}^*), and also the densities of Kr$^+$ ions (N_{Kr}^+) and Ar$^+$ ions (N_{Ar}^+). We consider the coupled photonic and electronic ionization pathways schematically shown in Fig. 2. These include three-photon ionization for the Kr-Ar mixture, $\omega_1 + \omega_1$ and $\omega_2 + \omega_3$ TPA Kr excitation followed by ω_1 one-photon ionization (or TPA followed by an electron impact ionization), electron impact excitation of Kr and Ar followed up by one-photon ionization, direct electron impact ionization, and also stepwise electron impact excitation followed also by electron impact ionization. Apart from these ionization pathways we also consider electron-ion recombination by a three-body collision and the deexcitation of Kr* and Ar* atoms due to collisions with electrons that have energy lower than that required for ionization.

For the Kr-Ar mixture with $J_{\mathrm{Kr}} = 14$ eV and $J_{\mathrm{Ar}} = 15.8$ eV we consider only the ionization effect by $\lambda_1 = 212.6$ nm photons in view of the approximately four orders of magnitude lower intensity of $\lambda_3 = 121.6$ nm radiation, the large number of photons required for ionization, and the low ionization probability for $\lambda_2 = 843$ nm radiation. The multiphoton ionization rate is given by [43–46]

$$W_{\mathrm{mpi}-k} \approx \omega_1 n_{\mathrm{ph}}^{3/2} \left(\frac{1}{2J_k} \frac{e^2 E_{01}^2}{4m\omega_1^2} \right)^{n_{\mathrm{ph}}}, \qquad (6)$$

where $k = $ Kr, Ar, $n_{\mathrm{ph}} = J_k/\hbar\omega_1$ is the number of photons necessary for atom ionization with J_{k} as the ionization energy, and $\varepsilon_{\mathrm{osc}} = e^2E_{01}^2/4m\omega_1^2$ is the related electron quiver energy with $E_{01}^2 = 2I_1/n_1\varepsilon_0 c$.

The process rates, associated with the electron impact excitation and ionization, are defined via the electron quiver energy [41,47],

$$\varepsilon_{\mathrm{osc}} \approx \frac{e^2E_{01}^2}{4m\omega_1^2} + \frac{e^2E_{02}^2}{4m\omega_2^2}, \qquad (7)$$

and include the electron density N_{e} multiplied by the characteristic frequency [40]:

$$\begin{aligned} \nu_{j-k} &= \frac{1}{\Delta J_{j-k}} \frac{d\varepsilon_{\mathrm{el}}}{dt} \\ &= \frac{1}{\Delta J_{j-k}} \left[\frac{e^2E_{01}^2\nu_c}{2m(\omega_1^2+\nu_c^2)} + \frac{e^2E_{02}^2\nu_c}{2m(\omega_2^2+\nu_c^2)} \right] \\ &\approx \frac{2\varepsilon_{\mathrm{osc}}\nu_c}{\Delta J_{j-k}} = R_{j-k}N_k, \end{aligned} \qquad (8)$$

with which the electrons, increasing their energy ($\varepsilon_{\mathrm{el}}$) in the laser field and making collisions with the atoms of Kr ($k = 1$) and Ar ($k = 2$), are able to overcome the corresponding energy barriers (denoted by j): $\Delta J_{j-k} = J_k$ (ionization of atoms, $j = 1$), $\Delta J_{j-k} = J_k^*$ (excitation of atoms, $j = 2$) or $\Delta J_{j-k} = J_k - J_k^*$ (ionization of excited atoms, $j = 3$), N_k is the related density of atoms, and $R_{j-k} = 2\varepsilon_{\mathrm{osc}}\sigma\bar{V}_{\mathrm{el}}/\Delta J_{j-k}$ are the related process rates.

The recombination rate due to the three-body collision, $\beta_e N_k^+ N_e^2$(s^{-1} cm^{-3}), depends on the recombination coefficient, $\beta_e N_e$. For a Kr-Ar density of the order of $\sim 10^{18}$ cm^{-3} and electron temperature $T_{\mathrm{e}} = 16\,000$ K, the value of $\beta_e \approx 5.9\times10^{-31}$ cm^6/s [41] giving the recombination time $\tau_r = 1/\beta_e N_e N_k^+ \approx 10^{-5}$ s $\gg \tau_{\mathrm{p}} \approx 1$ ns. However, for Kr-Ar density $\approx 10^{20}$ cm^{-3} considered here, $\tau_r = 1/\beta_e N_e N_k^+ < 10^{-9}$ s, suggesting that recombination should remain in the model. We can also estimate the diffusion coefficient for electrons as $D_e \approx \bar{V}_{\mathrm{el}}^2/3\nu_c = 3\times10^5$–$3\times10^4$ cm^2/s for $P_g = 10^4$–10^5 Pa and ($\bar{V}_{\mathrm{el}} \approx 10^8$ cm/s and $\nu_c = N_g\sigma\bar{V}_{\mathrm{el}} = 4\times10^{10}-10^{11}$ Hz). However, due to Coulomb interaction with ions the electron diffusion is defined by the ambipolar diffusion: $D_a \approx D_i(1 + T_e/T_i)$, where the diffusion of ions is similar to that of atoms, i.e., $D_i \approx 0.119/P_g$(at) cm^2/s and T_{i} is the ion temperature. For $P_{\mathrm{g}} \approx 10^4$–$10^5$ Pa one has $D_{\mathrm{i}} \approx 0.12$–$1.2$ cm^2/s. The characteristic time of electron collisions with ions is $\tau^* \approx \nu_c^{-1} = 1/N_g\sigma\bar{V}_{\mathrm{el}} \approx 0.01$–$0.1$ ns and the characteristic time for ion heating is of the order $\tau^* M/m_e \approx 1$ μs. Thus, during nanosecond pulses considered here the ions remain cold ($T_{\mathrm{i}} \approx 500$–$1000$ K) and one finds that for $\varepsilon_{\mathrm{el}} \approx 5$–$10$ eV $D_{\mathrm{a}} \approx 100 D_{\mathrm{i}} \approx 10$–$100$ cm^2/s. Therefore, the diffusion of electrons even from the smallest irradiated zone considered ($r_0 \approx 10$ μm) requires time $\approx r_0^2/D_a \approx 10$–$100$ ns $\gg \tau_{\mathrm{p}} \approx 1$ ns, and is, consequently, neglected in this study.

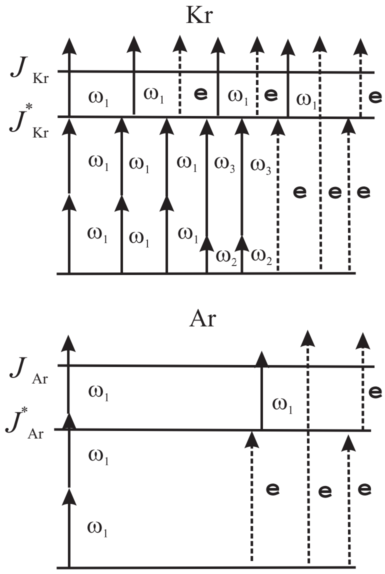

FIG. 2. Considered pathways of Kr and Ar ionization by photon and electron impacts (solid arrows correspond to a photon interaction and dashed arrows correspond to an electron interaction).

Finally, our model for electron, Kr and Ar ion densities is described by the following set of equations:

$$\begin{aligned}\frac{dN_e}{dt} &= W_{\mathrm{mpi-Kr}}N_{\mathrm{Kr}} + W_{\mathrm{mpi-Ar}}N_{\mathrm{Ar}} + R_{1-\mathrm{Kr}}N_{\mathrm{Kr}}N_e \\ &\quad + R_{1-\mathrm{Ar}}N_{\mathrm{Ar}}N_e + R_{2-\mathrm{Kr}}N^*_{\mathrm{Kr}}N_e + R_{2-\mathrm{Ar}}N^*_{\mathrm{Ar}}N_e \\ &\quad - \beta_{\mathrm{Kr}}N^+_{\mathrm{Kr}}N_e^2 - \beta_{\mathrm{Ar}}N^+_{\mathrm{Ar}}N_e^2 + W^*_{\mathrm{Kr}}N^*_{\mathrm{Kr}} + W^*_{\mathrm{Ar}}N^*_{\mathrm{Ar}},\end{aligned} \tag{9}$$

$$\begin{aligned}\frac{dN^+_{\mathrm{Kr}}}{dt} &= W_{\mathrm{mpi-Kr}}N_{\mathrm{Kr}} + R_{1-\mathrm{Kr}}N_{\mathrm{Kr}}N_e + R_{2-\mathrm{Kr}}N^*_{\mathrm{Kr}}N_e \\ &\quad - \beta_{\mathrm{Kr}}N^+_{\mathrm{Kr}}N_e^2 + W^*_{\mathrm{Kr}}N^*_{\mathrm{Kr}},\end{aligned} \tag{10}$$

$$\begin{aligned}\frac{dN^+_{\mathrm{Ar}}}{dt} &= W_{\mathrm{mpi-Ar}}N_{\mathrm{Ar}} + R_{1-\mathrm{Ar}}N_{\mathrm{Ar}}N_e + R_{2-\mathrm{Ar}}N^*_{\mathrm{Ar}}N_e \\ &\quad - \beta_{\mathrm{Ar}}N^+_{\mathrm{Ar}}N_e^2 + W^*_{\mathrm{Ar}}N^*_{\mathrm{Ar}}.\end{aligned} \tag{11}$$

where $R_{1-k} = 2\varepsilon_{\mathrm{osc}}\sigma_{i-k}\bar{V}_{\mathrm{el}}/J_k$, $R_{2-k} = 2\varepsilon_{\mathrm{osc}}\sigma_{i-k}\bar{V}_{\mathrm{el}}/(J_k - J_k^*)$, $W_k^* = \sigma_k^* I_1/\hbar\omega_1$ is the rate of linear absorption ionization of the excited Kr and Ar atoms ($k =$ Kr, Ar), and $\sigma_{i-k} \approx 2 \times 10^{-16}$ cm^2 is the cross-section constant for Kr and Ar ionization [41]. For $W_{\mathrm{mpi}-k}$ see Eq. (6).

Additionally, we write the rate equations for densities of Kr* and Ar* including the excitation and deexcitation pathways described above:

$$\begin{aligned}\frac{dN^*_{\mathrm{Kr}}}{dt} &= W_{\mathrm{TPA-Kr}}N_{\mathrm{Kr}} + R_{3-\mathrm{Kr}}N_{\mathrm{Kr}}N_e - R_{2-\mathrm{Kr}}N^*_{\mathrm{Kr}}N_e \\ &\quad - \beta_{D-\mathrm{Kr}}N^*_{\mathrm{Kr}}N_e - W^*_{\mathrm{Kr}}N^*_{\mathrm{Kr}},\end{aligned} \tag{12}$$

$$\begin{aligned}\frac{dN^*_{\mathrm{Ar}}}{dt} &= R_{3-\mathrm{Ar}}N_{\mathrm{Ar}}N_e - R_{2-\mathrm{Ar}}N^*_{\mathrm{Ar}}N_e \\ &\quad - \beta_{D-\mathrm{Ar}}N^*_{\mathrm{Ar}}N_e - W^*_{\mathrm{Ar}}N^*_{\mathrm{Ar}},\end{aligned} \tag{13}$$

where $W_{\mathrm{TPA-Kr}} = \beta_0 I_1^2(\mathbf{x},t)/\hbar\omega_1 N_{\mathrm{Kr0}}$ is the TPA excitation rate, $R_{3-k} = 2\varepsilon_{\mathrm{osc}}\sigma_{e-k}\bar{V}_{\mathrm{el}}/J_k^*$ is the excitation rate by electron collisions with the related cross section $\sigma_{e-k} \approx 10^{-16}$ cm^2 for Kr and Ar, $\beta_{D-\mathrm{Kr}} \approx \beta_{D-\mathrm{Ar}} = \sigma_D \bar{V}_{\mathrm{el}}$ is the deexcitation constant [41] with a cross section $\sigma_D \approx 10^{-17}$ cm^2, $N_k + N_k^* + N_k^+ = N_{k0}$, and for the initial conditions we have: $N_k = N_{k0}$, $N_k^* = N_k^+ = 0$ for $k =$ Kr, Ar.

The electron density changes the refractive indices from that of the neutral gas, $n_i = \sqrt{\varepsilon_i}$, to $n_i^* = \sqrt{\varepsilon_i^*} = (n_i^2 - \omega_p^2/\omega_i^2)^{1/2} \approx n_i - \omega_p^2/2\omega_i^2$, leading to a wave vector mismatch:

$$\Delta k = 2k_1 - k_2 - k_3 = \frac{1}{c}[2\omega_1 n_1^* - \omega_2 n_2^* - \omega_3 n_3^*], \tag{14}$$

where n_{i} depends also on the local Kr and Ar densities depleted by the ionization with time.

A rigorously coupled two-dimensional (2D) time-dependent simulation of this model is performed by using finite-difference 30×2000 discretization over *r*-*z* space and 20 000 discretization over *t* similar to that of Refs. [48–50].

IV. RESULTS AND DISCUSSION

This model allows one to simulate many important effects. We focus here on only the most interesting effects revealed by our study.

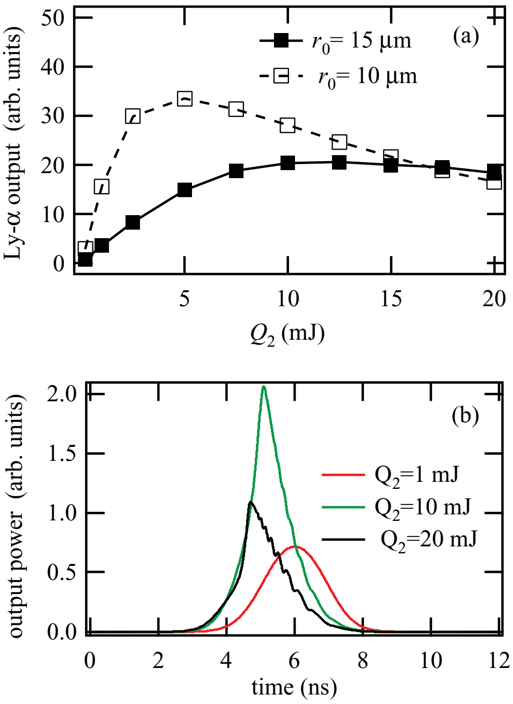

FIG. 3. (Color) (a) Output Ly-α energy versus Q_2 and (b) output Ly-α power versus time for $r_0 = 10$ μm.

First, this model allows one to understand the physical background of the related experimental data. In particular, we consider the saturation of the output Ly-α energy taking place with increase of 843-nm pulse energy observed in Ref. [36]. That is, Fig. 3 shows the simulation results for (a) the output Ly-α energy (arb. units) versus 843-nm pulse energy (Q_2) and (b) Ly-α related power (arb. units) versus time. The related Fig. 4 shows the simulation results for (a) the maximal electron

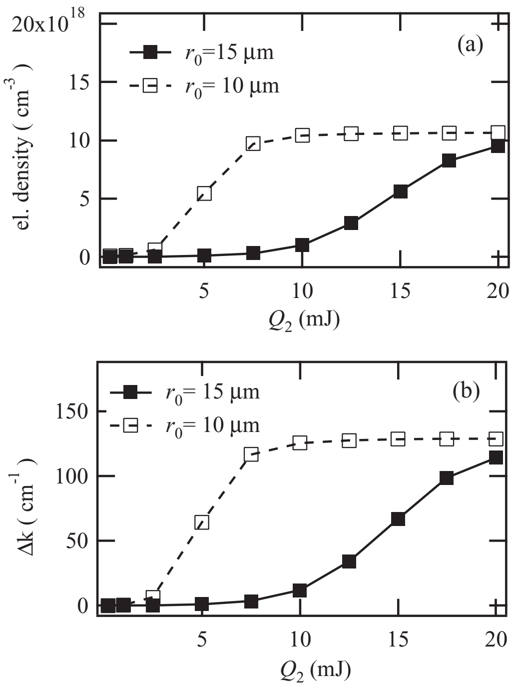

FIG. 4. (a) Electron density and (b) dephasing versus Q_2.

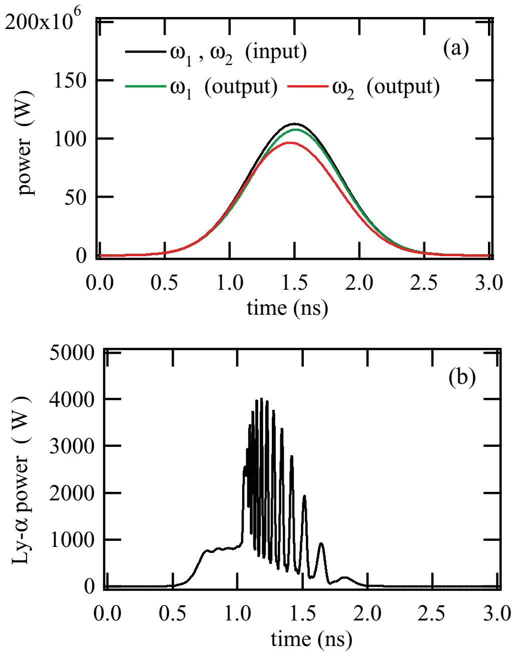

FIG. 5. (Color) Pulse powers for $Q_1 = Q_2 = 100$ mJ, $L = 10$ cm, $r_0 = 40$ μm, $P_{\mathrm{Kr}} = 10^4$ Pa, and $P_{\mathrm{Ar}} = 3.45\times10^4$ Pa: (a) fundamental input and output and (b) Ly-α output.

density and (b) dephasing Δk versus Q_2. The simulations are done for the following set of parameters: $Q_1 = 0.2$ mJ, $Q_2 = 0.2$–20 mJ, $r_0 = 10$–15 μm, $L = 10$ cm, $P_{\mathrm{Kr}} = 10^4$ Pa, $P_{\mathrm{Ar}} = 3.45\times10^4$ Pa, and pulse duration is 4 ns. Figure 3(a) shows the saturation of the generated Ly-α energy taking place with increasing $Q_2 = 0.2$–10 mJ. For $r_0 = 10$ μm this saturation takes place when $Q_2 \approx 5$ mJ, whereas for $r_0 = 15$ μm the saturation takes place when $Q_2 \approx 10$ mJ. The experimental data [36] show that for approximately similar pressure and beam radius parameters the saturation takes place for $Q_2 \approx 0.6$–8 mJ. The saturation is explained by the related electron density and dephasing plots versus Q_2 which are shown in Figs. 4(a) and 4(b). That is, the electron density achieves the level of $N_e \approx 10^{19}$ cm^{-3} corresponding to the full ionization of Kr-Ar gas. This ionization leads to the sharp dephasing and also to the sharp fall of $\chi^{(3)} = \chi^{(3)}_{a-\mathrm{Kr}} N_{\mathrm{Kr}}$.

Second, Fig. 3(b) also shows that with increase of Q_2 from 1 mJ to 20 mJ the output Ly-α power experiences the transition to auto-oscillations. These auto-oscillations become much stronger for larger input intensities. In particular, we consider also the case of 1-ns pulse mixing of a 100-mJ energy input of 212.6-nm and 843-nm radiation in the initially phase-matched ($\Delta k = 0$) Kr-Ar mixture: $P_{\mathrm{Kr}} = 10^4$–10^5 Pa per $P_{\mathrm{Ar}} = 3 - 6\times10^5$ Pa within the interaction length $L = 10$ cm for beam radii $r_0 = 40$–300 μm. The calculation presented in Fig. 5 shows (a) the fundamental input and output pulse powers and (b) the output Ly-α power as function of time for $Q_1 = Q_2 = 100$ mJ, $L = 10$ cm, $r_0 = 40$ μm, $P_{\mathrm{Kr}} = 10^4$ Pa, and $P_{\mathrm{Ar}} = 3.45\times10^4$ Pa. A simulated Ly-α pulse shows a rapid power increase followed by a drastic fall combined with strong auto-oscillations within a period of ~0.5 ns before the fundamental powers achieve their maximum (at $t = 1.5$ ns). Both fundamental beams experience strong absorption effect.

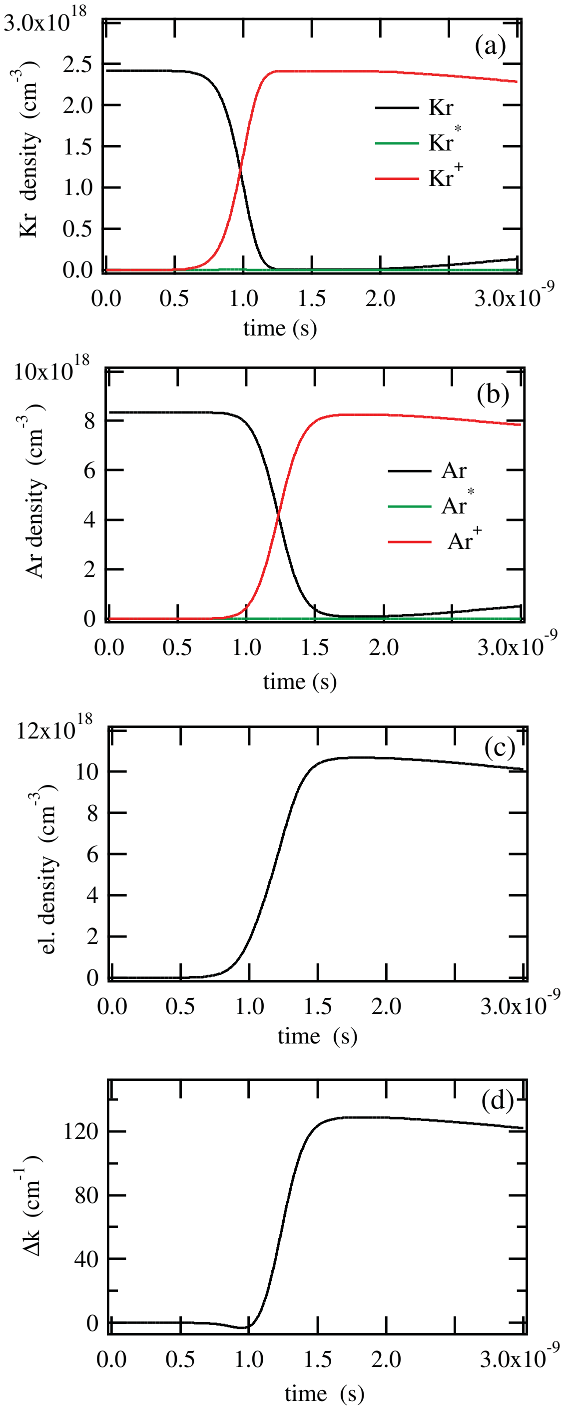

FIG. 6. (Color) Plasma generation for $Q_1 = Q_2 = 100$ mJ, $L = 10$ cm, $r_0 = 40$ μm, $P_{\mathrm{Kr}} = 10^4$ Pa, and $P_{\mathrm{Ar}} = 3.45\times10^4$ Pa: (a) Kr density, (b) Ar density, (c) electron density, and (c) related dephasing ($z = 0$ and $r = 0$).

The output pulse power inhibition and the onset of these auto-oscillations in the Ly-α pulse are explained by Fig. 6 where we show the time evolution of (a) Kr density, (b) Ar density, (c) electron density, and (d) Δk. In particular, Figs. 6(a) and 6(b) show Kr, Kr*, Kr$^+$ and Ar, Ar*, Ar$^+$ densities versus time. The ionization of Kr and Ar atoms and the electron avalanche [Fig. 6(c)] take place within a period of ~0.5 ns, when the onset of the auto-oscillations and the drastic fall in the

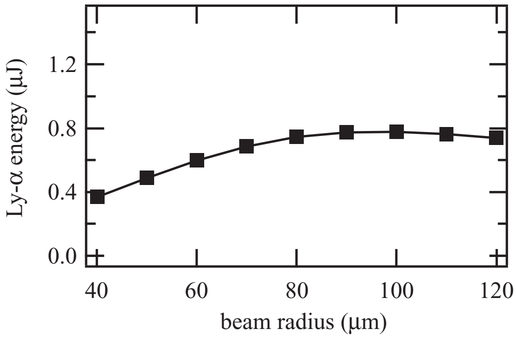

FIG. 7. Generated Ly-α pulse energy as function of beam radius for $P_{\mathrm{Kr}} = 10^4$ Pa and $P_{\mathrm{Ar}} = 3.45\times10^4$ Pa; $Q_1 = Q_2 = 100$ mJ.

Ly-α pulse power take place. Additionally, due to Kr excitation by TPA its ionization is found to occur ~0.3 ns earlier compared to the onset of Ar ionization. The recombination is found to be small for this case.

The oscillatory behavior in the Ly-α pulse intensity and power, $P_3 = 2\pi \int I_3 r dr$, can be qualitatively explained by considering a simplified analytical approximation [1]:

$$I_3 \propto \left(\chi_a^{(3)} N_{Kr}\right)^2 L^2 I_1^2 I_2 \sin^2(\Delta k L/2)/(\Delta k L/2)^2. \quad (15)$$

This equation suggests that the temporal change in Δk and $\sin^2(\Delta k L/2)/(\Delta k L/2)^2$ is responsible for the output Ly-α power decay and auto-oscillations. Apart from this, the strong Ly-α power decay is also associated with the decrease in $\chi^{(3)} = \chi_a^{(3)} N_{\mathrm{Kr}}$. These auto-oscillations disappear with a decrease of the input intensities and a related decrease of the electron density and dephasing.

Figure 7 shows the related dependence of the output Ly-α pulse energy versus beam radius. This figure shows that the output energy increases and saturates with an increase in radius. However, the output Ly-α pulse energy remains below 1 μJ and the resulting process efficiency is below 10^{-5}.

Third, the simulation presented in Figs. 8–11 is aimed towards conditions which can allow the operation with a higher output energy, stability, and efficiency. In particular Fig. 8 shows (a) fundamental input and output pulse powers and (b) output Ly-α pulse power as function of time for $Q_1 = Q_2 = 100$ mJ, $L = 10$ cm, $r_0 = 40$ μm, $P_{\mathrm{Kr}} = 10^5$ Pa, and $P_{\mathrm{Ar}} = 5.95\times10^5$ Pa. A simulated Ly-α pulse also shows a rapid power increase followed by a drastic fall also combined with the auto-oscillations within a period of ~0.5 ns before the fundamental powers achieve their maximum (at $t = 1.5$ ns). In this case the auto-oscillations are found to be significantly weaker as compared with the low-pressure case. However, in this case both fundamental powers show very strong absorption effect, caused, though, by different mechanisms. For 212.6-nm radiation the absorption is mainly due to TPA, whereas for 843-nm radiation the absorption is mainly due to the interaction with the free electrons appearing with the onset of ionization. That is, the onset of strong 843-nm radiation absorption at $t \approx 0.7$ ns corresponds exactly to the onset of strong ionization and electron avalanche shown in Fig. 9 where the time evolution of (a) Kr density, (b) Ar density, (c) electron density, and (d) Δk are given. In contrast with the previous low-gas-density case, for this case the numerical simulation shows the onset of significant recombination at the end of the pulse. Additionally, in this case the ionization develops much faster due to the higher electron-atom collision frequency, $\nu_c \approx (N_{\mathrm{Kr}} + N_{\mathrm{Ar}})\sigma \bar{V}_{\mathrm{el}}$, and Kr and Ar are ionized almost simultaneously.

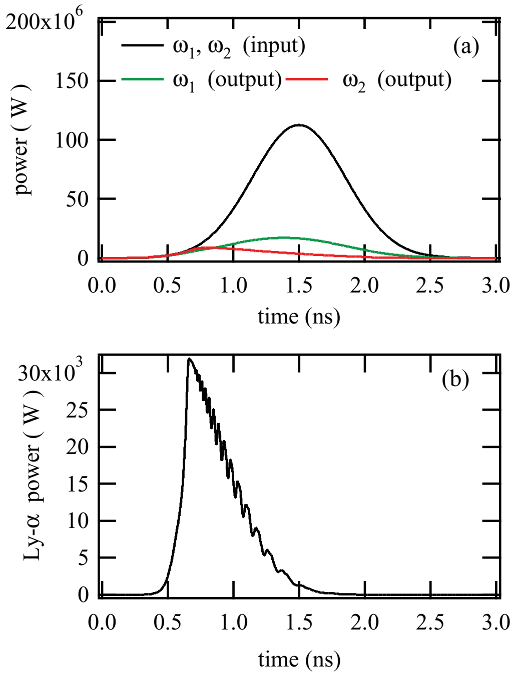

FIG. 8. (Color) Pulse powers for $Q_1 = Q_2 = 100$ mJ, $L = 10$ cm, $r_0 = 40$ μm, $P_{\mathrm{Kr}} = 10^5$ Pa, and $P_{\mathrm{Ar}} = 5.95\times10^5$ Pa : (a) fundamental input and output and (b) Ly-α output.

Figure 10 shows the time evolution of (a) Ly-α power and (b) related dephasing value Δk for $Q_1 = Q_2 = 100$ mJ, $L = 10$ cm, $P_{\mathrm{Kr}} = 10^5$ Pa, and $P_{\mathrm{Ar}} = 5.95\times10^5$ Pa for various beam radii $r_0 = 40$–280 μm. These figures are shown to demonstrate that the auto-oscillations tend to decay with increase in r_0, decrease of laser input intensities, and the generated electron density and resulting dephasing Δk. In particular, the auto-oscillations are found to decay for $r_0 \approx 160$ μm and to disappear for $r_0 \approx 280$ μm when the electron density and Δk remain low during the pulse, and increase only by the end of the pulse. For large diameters the maximum in Ly-α pulse power shifts towards the maxima of the fundamental powers, i.e., towards $t = 1.5$ ns.

Figure 11 shows the simulated Ly-α pulse energy for $P_{\mathrm{Kr}} = 10^5$ Pa and $P_{\mathrm{Ar}} = 5.95\times10^5$ Pa: (a) versus radius r_0 for $L = 10$ cm and (b) versus L for $r_0 = 240$ μm. Figure 11(a) (solid line) demonstrates that with the increase of pulse intensity (with decrease in r_0) the output Ly-α pulse energy increases, reaches saturation, and then decreases. The maximum Ly-α pulse energy ~29 μJ corresponds to $r_0 \approx 240$ μm with the final efficiency ~3×10^{-4}. Figure 11(b) demonstrates that the output Ly-α pulse energy increases, saturates, and decreases with increase in L. The saturation takes place due to TPA which compensates the increase of the output energy with increase of the interaction length. The maximal output Ly-α pulse energy is found to achieve ~50 μJ with a resulting efficiency of 5×10^{-4}.

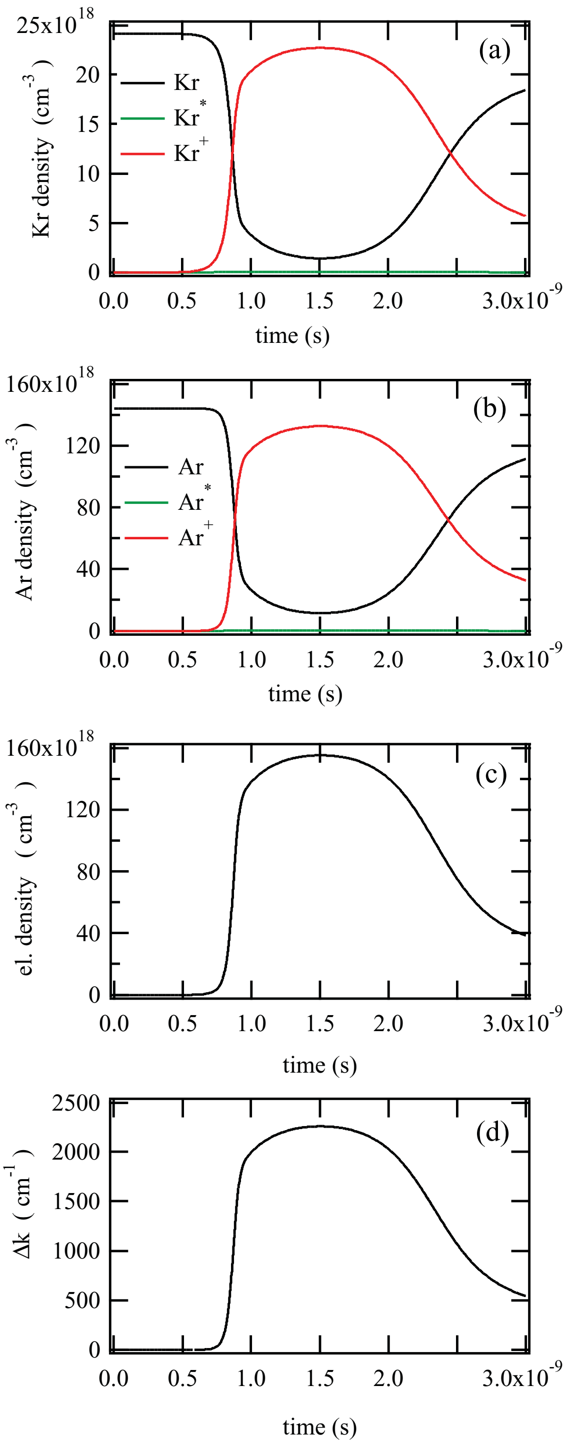

FIG. 9. (Color) Plasma generation for $Q_1 = Q_2 = 100$ mJ, $L = 10$ cm, $r_0 = 40$ μm, $P_{\mathrm{Kr}} = 10^5$ Pa, and $P_{\mathrm{Ar}} = 5.95\times10^5$ Pa: (a) Kr density, (b) Ar density, (c) electron density, and (c) related dephasing ($z = 0$ and $r = 0$).

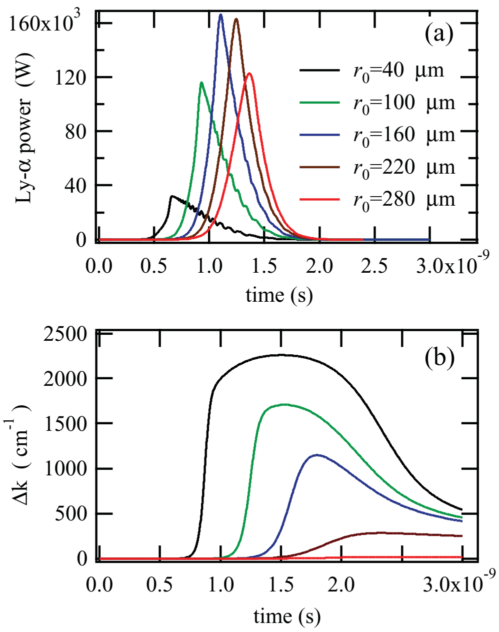

FIG. 10. (Color) (a) Pulse power and (b) dephasing versus time for various beam radii ($z = 0$ and $r = 0$).

Additionally, Fig. 11(a) shows that in the considered process the resulting efficiency is strongly restricted by $\omega_1 + \omega_1$ TPA. That is, the output Ly-α pulse energy is shown in this figure for two values of TPA cross section, $\sigma^{(2)} \approx 2.5\times10^{-50}$ cm^4 s/photon^2 (solid line) and $\sigma^{(2)} \approx 10^{-50}$ cm^4 s/photon^2 (broken line). For $\sigma^{(2)} \approx 10^{-50}$ cm^4 s/photon^2 the output energies are found to be about two times higher and the maximum shifts towards $r_0 \approx 180$ μm as compared with the case of $\sigma^{(2)} \approx 2.5\times10^{-50}$ cm^4 s/photon^2. It should be stressed here that this effect is primarily associated with a TPA resonance of 212.6-nm radiation and related

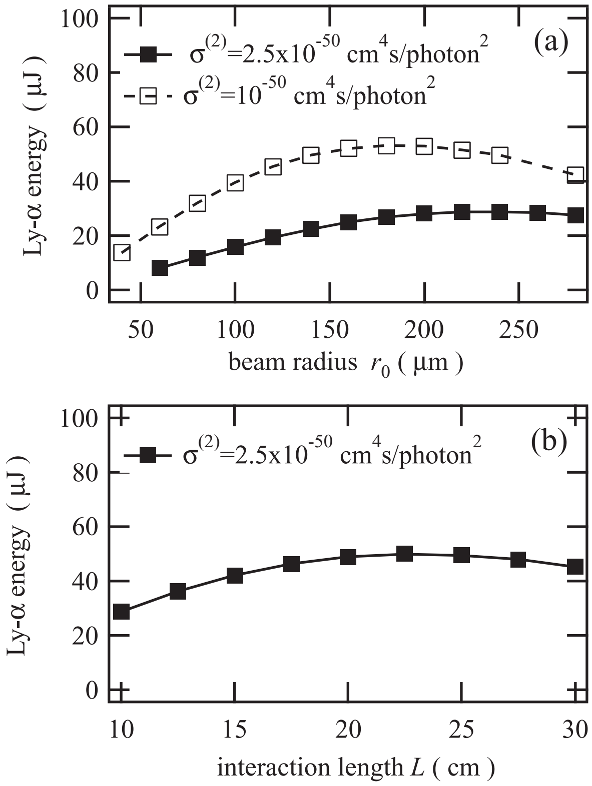

FIG. 11. Generated Ly-α pulse energy for $Q_1 = Q_2 = 100$ mJ, $P_{\mathrm{Kr}} = 10^5$ Pa, and $P_{\mathrm{Ar}} = 5.95\times10^5$ Pa as a function of (a) beam radius for $L = 10$ cm and (b) interaction length for $r_0 = 240$ μm.

Kr excitation, which provides the effective pathway for subsequent ionization. Second, a significant contribution to the inhibition of the Ly-α output energy is due to $\omega_2 + \omega_3$ TPA involving one photon of the generated Ly-α radiation and one photon of 843-nm radiation. However, its contribution to Kr excitation and ionization remains relatively low compared with that of 212.6-nm radiation.

Our simulations show that the resonant TPA Kr excitation followed by one-photon ionization is the main pathway for the initial ionization. This can be explicitly shown by simplifying Eq. (9) for the initial stage of the pulse as

$$\frac{dN_e}{dt} \approx W_{\mathrm{mpi-Kr}} N_{\mathrm{Kr}} + W_{\mathrm{mpi-Ar}} N_{\mathrm{Ar}} + W^*_{\mathrm{Kr}} N^*_{\mathrm{Kr}}, \qquad (16)$$

where the density of Kr excited by TPA is reduced to

$$\frac{dN^*_{\mathrm{Kr}}}{dt} \approx W_{\mathrm{TPA-Kr}} N_{\mathrm{Kr}}. \qquad (17)$$

In order to make explicit order of magnitude estimates let us assume that the intensity, $I_1 \approx Q_1/\pi r_0^2 \tau_p$ is constant over the pulse duration, $N^*_{\mathrm{Kr}}(t) \approx W_{\mathrm{TPA-Kr}} N_{\mathrm{Kr}} t$ and, therefore, the rate of electron generation is given by

$$\frac{dN_e}{dt} \approx W_{\mathrm{mpi-Kr}} N_{\mathrm{Kr}} + W_{\mathrm{mpi-Ar}} N_{\mathrm{Ar}} + W^*_{\mathrm{Kr}} W_{\mathrm{TPA-Kr}} N_{\mathrm{Kr}} t. \qquad (18)$$

We construct estimates for a pulse $Q_1 = 100$ mJ of $\tau_{\mathrm{p}} =$ 1 ns duration with beam radius $r_0 = 100$ μm giving $I_{01} \approx 3.2 \times 10^{11}$ W/cm^2, $E_{01} \approx 19\sqrt{I_{01}} \approx 1.1 \times 10^7$ V/cm and $\varepsilon_{\mathrm{osc}} = e^2 E_{01}^2 / 4m\omega_1^2 \approx 10^{-22}$ $J = 6.3 \times 10^{-4}$ eV. For Kr ionization energy $J_{\mathrm{Kr}} = 14$ eV we find $W_{\mathrm{mpi-Kr}} \approx 2.4 \times 10^5$ s^{-1} whereas for Ar $J_{\mathrm{Ar}} = 15.8$ eV and we find $W_{\mathrm{mpi-Ar}} \approx 8.3 \times 10^4$ s^{-1}. For $\sigma^{(2)} \approx 2.5 \times 10^{-50}$ cm^4 s/photon^2 and for $N_{\mathrm{Kr0}} = 2.4 \times 10^{19}$ cm^{-3} one has $\beta_0 \approx \sigma^{(2)} N_{\mathrm{Kr0}}/\hbar\omega_1 \approx 6.5 \times 10^{-13}$ cm/W and, therefore, for the TPA excitation rate of Kr one has $W_{\mathrm{TPA-Kr}} = \beta_0 I_{01}^2/\hbar\omega_1 N_{\mathrm{Kr0}} \approx 3 \times 10^9$ s^{-1}. For the one-photon ionization of the TPA excited Kr one has $W_k^* = \sigma_k^* I_1/\hbar\omega_1 \approx 1.4 \times 10^{12}$ s^{-1}. Thus, after 0.01 of pulse duration, i.e. $t = 0.01$ ns the rate of $(2 + 1)$-photon ionization, $W^*_{\mathrm{Kr}} W_{\mathrm{TPA-Kr}} t \approx 3 \times 10^9 \times 1.4 \times 10^{12} \times 10^{-11} = 4.2 \times 10^{10}$ s^{-1}, becomes much higher than $W_{\mathrm{mpi-Kr}} \approx 2.4 \times 10^5$ s^{-1}. We should also stress here that while the ionization is mainly initiated via $(2 + 1)$-photon ionization of Kr by 212.6-nm radiation, the electron avalanche develops mainly due to the effect of 843-nm radiation. That is, Eq. (7) shows that for the same intensities $E_{01} = E_{02}$ the avalanche effect of 843-nm laser radiation is $\omega_1^2/\omega_2^2 \approx 16$ times stronger as compared with that of 212.6 nm. Additionally the higher the pressure the faster the avalanche develops. This happens because the higher the pressure the shorter the time of all electron-Kr and electron-Ar collision pathways involved in the ionization [see Eq. (8)].

Finally, we should add that in addition to these auto-oscillations under high intensities the four-wave mixing process can also be prone to destabilizing lensing effects, associated with the radial gradients of the electron density and refractive indices, and also to the laser beam filamentation when the incident laser power significantly exceeds the related critical power. These effects can be estimated by using the radial distributions of refractive indices from the present model. In particular, the simulation shows that with the onset of electron avalanche the beam defocusing can take place due to decrease of the refractive indices on the beam axis, $n_i^* \approx n_i - \omega_p^2/2\omega_i^2$. In this connection, we also should note that for nanosecond pulses the relatively slow electron diffusion across the beam radius allows one to maintain the electron distribution conformal to the input laser energy beam distributions. Therefore, the lensing effects can be inhibited by using Π-type laser energy beams distributions made, for instance, by using adaptive optics systems.

V. SUMMARY AND CONCLUSIONS

We have developed a coupled model for simulation of the complex nonlinear optical process for four-wave mixing under optical discharge in which the ionization and electron avalanche equations are integrated together with optical equations. In our model we take into account change of the refractive indices, the related phase matching condition, and all other optical properties during the pulse.

This model gives reasonably good agreement with the experimental data for Ly-α radiation generation and elucidates the related mechanism of inhibition of Ly-α radiation by the resonant sum-difference mixing of 212.6-nm and 843-nm radiation. In particular, the simulations and analysis suggest that the employment of resonant enhancement of Ly-α generation leads also to dramatic enhancement of the photoionization via resonant TPA excitation of Kr followed by one-photon ionization which leads to fast avalanche ionization and breakdown of the initial phase-matching condition.

Additionally, we have performed a detailed numerical study of high-intensity sum-difference mixing for generation of Ly-α radiation in Kr-Ar gas for various operating conditions. The simulations show that in the high-intensity regime the generated Ly-α pulse can be prone to power auto-oscillations. These auto-oscillations are due to the electron avalanche caused by (i) initial electron generation by $(2 + 1)$-photon ionization of Kr by 212.6-nm radiation, (ii) electron impact excitation and ionization of Kr and Ar atoms with electron avalanche dominated by 843-nm radiation, and (iii) the breakdown of the optical phase-matching condition, $\Delta k = 2k_1 – k_2 – k_3 = 0$, and temporal evolution of Δk during the pulse.

Our simulation and analysis also show that all electron-Kr and electron-Ar collision pathways involved in electron avalanche are mainly due to the 843-nm laser which is $\omega_1^2/\omega_2^2 \approx 16$ times stronger as compared with that of 212.6 nm. Our study shows that, depending on pressure and other conditions the electron avalanche can be effectively inhibited by decreasing the intensity of the 843-nm radiation. In contrast, the reduction of 212.6-nm radiation appears ineffective for electron avalanche inhibition, additionally leading to a very detrimental loss in the output power.

Finally, let us stress that the proposed mechanism for auto-oscillations can develop also without exciting resonant TPA by 212.6-nm radiation, and can also be relevant to a variety of other nonlinear laser wave mixing processes in gases operating near the optical discharge threshold.

[1] J. F. Reintjes, *Nonlinear Optical Parametric Processes in Liquids and Gases* (Academic, London, 1984), and references therein.

[2] R. W. Boyd, *Non-linear Optics*, 2nd ed. (Academic, London, 2003), and references therein.

[3] H. Puell, H. Scheingraber, and C. R. Vidal, Phys. Rev. A **22**, 1165 (1980).

[4] M. S. Malcuit, D. J. Gauthier, and R. W. Boyd, Phys. Rev. Lett. **55**, 1086 (1985).

[5] R. W. Boyd, M. S. Malcuit, D. J. Gauthier, and K. Rzażewski, Phys. Rev. A **35**, 1648 (1987).

[6] S. E. Harris, J. E. Field, and A. Imamoğlu, Phys. Rev. Lett. **64**, 1107 (1990).

[7] K.-J. Boller, A. A. Imamoğlu, and S. E. Harris, Phys. Rev. Lett. **66**, 2593 (1991).

[8] K. H. Hahn, D. A. King, and S. E. Harris, Phys. Rev. Lett. **63**, 2777 (1990).

[9] C. Dorman and J. P. Marangos, Phys. Rev. A **58**, 4121 (1998).

[10] C. Dorman, I. Kucukkara, and J. P. Marangos, Phys. Rev. A **61**, 013802 (1999).

[11] M. Fleischhauer, A. Imamoglu, and J. P. Marangos, Rev. Mod. Phys. **77**, 633 (2005).

[12] K. S. E. Eikema, J. Walz, and T. W. Hänsch, Phys. Rev. Lett. **83**, 3828 (1999).

[13] K. S. E. Eikema, J. Walz, and T. W. Hänsch, Phys. Rev. Lett. **86**, 5679 (2001).

[14] A. Pahl, P. Fendel, B. R. Henrich, J. Walz, T. W. Hänsch, and K. S. E. Eikema, Laser Phys. **15**, 46 (2005).

[15] D. Kielpinski, Phys. Rev. A **73**, 063407 (2006).

[16] M. Sheid, D. Kolbe, F. Markert, T. W. Hänsch, and J. Walz, Opt. Express **17**, 11274 (2009).

[17] J. X. Yan, A. Dacrouri, M. Laroussi, and M. C. Gupta, J. Vac. Sci. Technol. **20**, 2574 (2002).

[18] B. D. Patterson, Rev. Mod. Phys. **60**, 69 (1988).

[19] Y. Miyake, J. P. Marangos, K. Shimomura, P. Birrer, T. Kuga, and K. Nagamine, Nucl. Instrum. Methods Phys. Res., Sect. B **95**, 265 (1995).

[20] P. Bakule and E. Morenzoni, Contemp. Phys. **45**, 203 (2004).

[21] P. Bakule, Y. Matsuda, Y. Miyake, K. Nagamine, M. Iwasaki, Y. Ikedo, K. Shimomura, P. Strasser, and S. Makimura, Nucl. Instrum. Methods Phys. Res., Sect. B **266**, 335 (2008).

[22] T. Nakajima, Opt. Express **18**, 27468 (2010).

[23] R. Mahon, T. J. Mcilrath, and D. W. Koopman, Appl. Phys. Lett. **33**, 305 (1978).

[24] R. Mahon, T. J. Mcilrath, V. P. Myerscough, and D. W. Koopman, IEEE J. Quantum Electron. **QE-15**, 444 (1979).

[25] J. P. Marangos, N. Shen, H. Ma, M. H. R. Hutchinson, and J. P. Connerade, J. Opt. Soc. Am. B **7**, 1254 (1990).

[26] K. D. Bonin and T. J. Mcllrath, J. Opt. Soc. Am. B **2**, 527 (1985).

[27] G. Hilber, A. Lago, and R. Wallenstein, J. Opt. Soc. Am. B **4**, 1753 (1987).

[28] R. Mahon and Y. M. Yiu, Opt. Lett. **7**, 279 (1980).

[29] G. W. Faris, S. A. Meyer, M. J. Dyer, and M. J. Banks, J. Opt. Soc. Am. B **17**, 1856 (2000).

[30] J. F. Ward and G. H. C. New, Phys. Rev. **185**, 57 (1969).

[31] G. C. Bjorklund, IEEE J. Quantum Electron. **QE-11**, 287 (1975).

[32] A. V. Smith, W. J. Alford, and G. R. Hadley, J. Opt. Soc. Am. B **5**, 1503 (1988).

[33] D. S. Bethune and C. T. Rettner, IEEE J. Quantum Electron. **QE-23**, 1348 (1987).

[34] G. Hilber, D. J. Brink, A. Lago, and R. Wallenstein, Phys. Rev. A **38**, 6231 (1988).

[35] S. Hannemann, U. Hollenstein, E.-J. van Duijn, and W. Ubachs, Opt. Lett. **30**, 1494 (2005).

[36] P. Bakule, Y. Matsuda, Y. Miyake, P. Strasser, K. Shimomura, S. Makimura, and K. Nagamine, Spectrochim. Acta, Part B **58**, 1019 (2003).

[37] A. M. Zheltikov and N. I. Koroteev, Phys.-Usp. **42**, 321 (1999).

[38] I. Strashnov, D. J. Blagburn, N. Thonnard, and J. D. Gilmour, Opt. Commun. **282**, 966 (2009).

[39] K. H. Becker, P. F. Kurunczi, and K. H. Schoenbach, Phys. Plasmas **9**, 2399 (2002).

[40] Yu. Raizer, *Laser-Induced Discharge Phenomena* (Consultants Bureau, New York, 1977), and references therein.

[41] Ya. B. Zel'dovich and Yu. P. Raizer, *Physics of Shock Waves and H-Ttemperature Hydrodynamics Phenomena* (Dover, Mineola, NY, 2002).

[42] H. A. Hyman, Appl. Phys. Lett. **31**, 14 (1977).

[43] L. V. Keldysh, Sov. Phys. JETP **20**, 1307 (1965).

[44] Y. A. Il'insky and L. V. Keldysh, *Electromagnetic Response of Materials Media* (Plenum, New York, 1994).

[45] B. Luther-Davies, E. G. Gamaly, Y. Wang, A. V. Rode, and V. T. Tikhonchuk, Sov. J. Quantum Electron. **22**, 289 (1992).

[46] E. G. Gamaly, A. V. Rode, B. Luther-Davies, and V. T. Tikhonchuk, Phys. Plasmas **9**, 949 (2002).

[47] In this equation, the term associated with the fields combined effect, $\propto e^2 E_{01} E_{02}/4m\omega_1\omega_2$, is found to be negligibly small.

[48] O. A. Louchev, N. E. Yu, S. Kurimura, and K. Kitamura, Appl. Phys. Lett. **87**, 131101 (2005).

[49] O. A. Louchev, N. E. Yu, S. Kurimura, and K. Kitamura, J. Appl. Phys. **98**, 113103 (2005).

[50] O. A. Louchev and S. Wada, J. Appl. Phys. **106**, 093106 (2009).